metals

MDPI

Article

The Correlation between Texture Evolution and Recrystallization Behavior during Rheologic Forming of 2195 Al–Li Alloy Cylindric Shell

Xiaona Wang [1], Wei Xiong [1], Ying Zheng [1,*] and Jin Zhang [1,2]

1 Light Alloy Research Institute, Central South University, Changsha 410083, China
2 State Key Laboratory of High Performance and Complex Manufacturing, Central South University, Changsha 410083, China
* Correspondence: 203812031@csu.edu.cn

Abstract: Spinning extrusion forming (SEF) is a type of rheologic forming process for making complex structured aerospace components, such as ribbed cylindric shells. However, our understanding of the texture evolution and recrystallization behavior during the SEF process is still limited, especially in complex system like the 2195 Al–Li alloy, which is considered to be the ideal material candidate for aerospace vehicles because of its low density and high specific strength. In this study, we investigate the microstructural evolution of a 2195 Al–Li alloy-made cylindric shell component during SEF and subsequent solution treatment and discuss the recrystallization mechanism and its influence on the texture. It is found that particle-stimulated nucleation (PSN) occurs during the SEF process due to a large number of Al_2Cu particles, which is responsible for the obvious reduction of texture components during SEF. Additionally, we show that the continuous dynamic recrystallization is responsible for the increased grains with {110} orientation, resulting in relatively stable brass texture components, even in the subsequent solution treatment.

Keywords: spinning extrusion forming; Al–Li alloy; texture; recrystallization

check for updates

Citation: Wang, X.; Xiong, W.; Zheng, Y.; Zhang, J. The Correlation between Texture Evolution and Recrystallization Behavior during Rheologic Forming of 2195 Al–Li Alloy Cylindric Shell. *Metals* **2023**, *13*, 853. https://doi.org/10.3390/met13050853

Academic Editor: Håkan Hallberg

Received: 30 March 2023
Revised: 22 April 2023
Accepted: 24 April 2023
Published: 27 April 2023

1. Introduction

The third generation Al–Li alloys have low density and high specific strength and stiffness and have been used in many important aerospace applications, including the cylindric shell, which is an essential component for high-performance launch vehicles [1–3]. The spinning extrusion forming (SEF) process is a newly developed rheologic forming approach for manufacturing ribbed cylindric shells which involves the spinning of a ring-shaped metal billet in various passes to extrude the rib structures [4]. The SEF process features a near-net-shape rheologic forming process, which addresses the problem of structural discontinuity during machining and internal stress concentration caused by welding [5]. However, the strong anisotropy of spin-extruded Al–Li alloy cylindric shells severely limits their further application as aerospace components [6–8].There are many factors affecting the anisotropy, of which the crystal texture is the most significant one [9,10] because the precipitated phase is precipitated along a specific orientation. In Al–Li alloy, the T1 phase with the best strength improvement precipitates along the {111} slip plane in dislocation entanglement and subgrain boundary. Due to the Schmid factor (SF) difference of deformation texture at a specific slip plane, the dislocation density generated by shear slip in the four precipitated {111} planes of the T1 phase is inhomogeneous during pre-deformation [11], which leads to the heterogeneity of the T1 phase at different slip planes, and finally leads to significant anisotropy. Some studies illustrate that the stacking fault energy of Al–Li alloy is relatively low, and the deformed texture can produce brass relatively easily [12], which not only causes the high anisotropy, but also affects the fracture properties of the components. It is studied to improve the deformation texture of Al–Li alloy by adjusting the temperature and strain rate [13,14]. In the experiment of Bate et al. [14], it was found that the brass texture of Al–Li alloy weakened with the increase of superplastic-forming strain during superplastic forming, which was closely related to the influence of grain boundary slip and grain growth on orientation. In addition, the change of texture of 2195 Al–Li alloy was discussed with respect to the recrystallization and particle dissolution, and it was found that the {011} <311> orientation texture weakened the anisotropy of the component [15]. Different original microstructure and orientation combinations due to the different SF will lead to different forming textures, while SEF uses the as-rolled blank to form the rib, and the evolution of the rolling texture in SEF has not been reported.

There have been numerous studies on controlling the deformation texture, mostly via the careful tunning of the secondary-phase and recrystallization behavior of the material [16–20]. It is known that secondary-phase particles are rich in Al–Li alloys and vary greatly in terms of their shape, size, and distribution, this significantly affects slipping behavior of dislocations during plastic deformation, resulting in different textures. For instance, the coarsened T1(Al_2CuLi) phase often leads to <001>//ND texture [17], distortion around S (Al_2CuMg) phase is believed to enhance the brass texture [18], and δ′ (Al_3Li) phase causes strong plane slip during deformation, resulting in a strong brass texture [19]. Interestingly, there are also studies suggesting that secondary-phase particles could suppress the deformation texture through other mechanisms, such as particle-stimulated nucleation (PSN), where the dislocation slip is hindered by non-deformable particles and thus increases the distortional energy around them, this mechanism gives rise to randomly-oriented recrystallized grains [20]. Moreover, the size and shape of the secondary-phase particles deeply affect the degree of local uneven deformation and the amount of recrystallization, thus showing different abilities to weaken the texture [21].

In addition, it is known that solution treatment has a great influence on the texture components, For example, Wang [22] showed that the texture and the anisotropy of hot extruded Al–Mg–Si plate has been weakened after the solution treatment, whereas in extruded 2196 Al–Cu–Li alloy, the type and fraction of the texture components barely change in the subsequent solution treatment [23], and in multi-directionally forged Al–Cu–Mg alloy, it was found that solution treatment even enhances the texture [24]. Wang showed that different recrystallization behaviors lead to different variation tendencies of texture components [25]. By controlling the rolling temperature, Liu et al. [26] analyzed the influence of different final rolling temperatures on the recrystallization degree in solid solution treatment, which led to the formation of different texture components. In addition, temperature-induced recrystallization is very fast in annealing, which leads to the possibility of PSN before particle dissolution. Although in previous studies, PSN during polycrystalline deformation easily produces randomly oriented nuclei and lead to texture diffusion, some studies have found that PSN may lead to the recrystallization of texture during annealing [27]. This adds another layer of uncertainty to the mechanism behind the texture evolution of Al–Li alloys, considering the complex configuration of secondary phases and microstructures in Al–Li alloys.

In order to elucidate the above questions, here, we studied the microstructure and texture evolution of 2195 Al–Li alloy cylindric shell during the SEF process and subsequent solution treatment. The mechanisms behind the texture evolution and recrystallization behavior at different stages are investigated. The effects of various secondary phases on the texture components and recrystallization behaviors during the process are discussed.

2. Materials and Methods

An as-rolled 2195 Al–Li alloy sheet was spinning-extruded to form an arc-shaped sheet (170 mm) with a curvature radius of 1.125 m; this is to simulate the local forming conditions on a 2.25 m-diameter cylindric shell for a rocket launcher and to investigate the material behaviors during processing and solution treatment. The as-rolled plate is milled into a blank of 230 × 150 × 5 mm, as shown in Figure 1. The middle boss of the blank is a forming part with a thickness of 5 mm. In order to avoid the excessive influence of clamping at both ends on axial elongation and simulate the radial constraint of the cylinder, the height of the clamping part is milled to 2 mm.

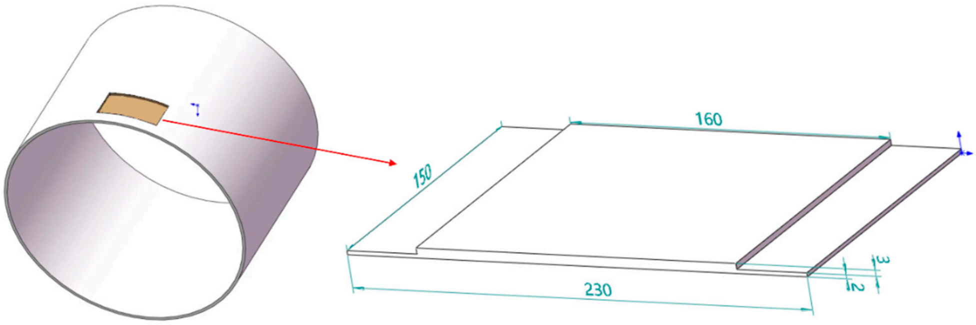

Figure 1. Blank and its size.

The SEF device is shown in Figure 2. It consists of a spinning wheel, a mold, a clamp for restraining the axial direction and the radial direction, a heating device, and a thermocouple connected with a temperature feedback device; a constant temperature heating state is maintained during the forming.

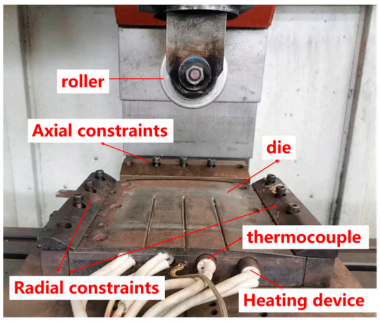

Figure 2. Spinning extrusion forming (SEF) reduced-scale device.

The SEFed ribbed sheet is shown in Figure 3a. During the SEF process, a total thickness reduction of 40% was completed in two steps at 300 °C (denoted as SEF-20 and SEF-40). In the forming process, the spinning wheel is fed in the direction perpendicular to the rib (TD). The radial feed direction is the same in the same pass, and the radial feed direction is changed between different passes. The blank and the die are preheated for two hours before SEF. The SEFed arc-shaped sheet was then solution treated at 510 °C for 1 h.

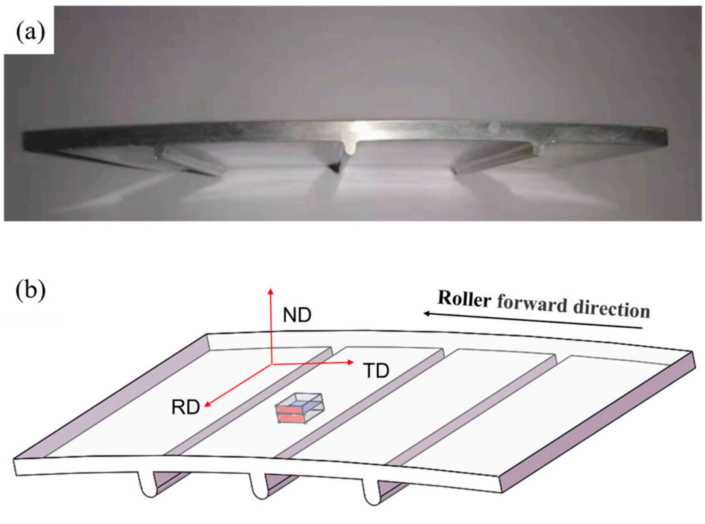

Figure 3. (**a**) Arc-shaped ribbed sheet after SEF; (**b**) sampling regions of EBSD specimens.

The grain orientations and microstructure of the sheet at different stages of SEF processing and solution treatment were studied by electron backscattering diffraction (EBSD, NordlysMax2, Oxford Instruments, Oxfordshire, UK) in a scanning electron microscope (SEM, MIRA4 LMH, TESCAN, Brno, Czechia). The second-phase fraction is calculated using Image J. It has been reported that the general reverse shear is superimposed on the plane strain, which leads to the uneven surface structure and coarse crystal layer of the rolled sheet [28]. So, EBSD specimens were cut from the central region in order to avoid the tensile deformation caused by the edge constraint and the difference microstructure near the rib, and, observed along TD–ND plane (see Figure 3b, marked red), the specimens were first manually polished and then electropolished in the solution of 90% ethanol (C_2H_5OH) and 10% perchloric acid ($HClO_4$) under a voltage of 20 V. The scanning image corresponding to EBSD around the second-phase particles was obtained by the secondary electrons. A scanning step size of 0.5 μm at a voltage and a beam current of 2.7 nA, as well as the magnification of 1000, was used to acquire the microstructural characteristics. EBSD data were analyzed using Channel 5. Grain boundaries of 2–5° were defined as sub-grain boundaries (SGBs), grain boundaries of 5–15° (including 5°) were defined as low angle grain boundaries (LAGBs), and grain boundaries higher than 15° were defined as high angle grain boundaries (HAGBs). The area fraction of each texture component applied a 15° deviation from the true {hkl} <uvw> orientation. The secondary phases and dislocation configurations were studied by transmission electron microscope (TEM, Talos F200X S/TEM, Nanoscience Instruments, Phoenix, AZ, USA) and STEM-EDS (Super-X). TEM samples were taken from the thickness center (see Figure 3b, marked purple) and first thinned below 80 μm then electropolished by a twin-jet electropolishing device, using a mixture of HNO_3 and CH_4O (3:7 in volume) at a voltage of 15 V at −30 °C.

3. Results

3.1. Grain Configuration in Different Forming Stages

Figure 4 shows the inverse pole figures (IPF) and corresponding Grain Orientation Spread (GOS) of the SEFed sheet at different stages, where LAGBs are marked white and HAGBs are black. Grain with GOS < 2.5° is defined as recrystallization, blue grains are recrystallization grains, red grains are deformed grains, and yellow grains are subgrain grains. In addition, the more obvious line width is used in the GOS diagram to show the distribution details of subgrain boundary. For the as-rolled sheet, lathy structure of various orientations can be observed, with uneven thickness along the transverse direction (Figure 4a). A large number of substructures can be seen inside the grains. After the first pass of SEF process, 20% thickness reduction was achieved (as shown in Figure 4b), the size of the lathy grains is reduced from 4.55 μm to 3.2 μm, and some recrystallized grains were formed (Figure 4f). The fraction of recrystallized grains increased from 4.6% after rolling to 7.2% after SEF-20. After SEF-40, the total thickness was reduced by 40% (as shown in Figure 4c), the lamellar structure was mostly broken up and the fraction of recrystallized grains was significantly increased (20%) (Figure 4g). This abrupt increase of recrystallized grains is usually related to a higher thinning rate, for the first pass of the SEF, the thickness of the sheet was reduced from 5 mm to 4 mm (20%), whereas for the second pass, it is reduced from 4 mm to 3 mm (25%). The higher thinning rate in the second pass leads to the higher degree of recrystallization, this has also been reported by Jurij J., Sidor [29], and Li [30]. After solution treatment, the thickness of the lamellar grains increased, but a large number of LAGBs (Figure 4h) can still be observed within the grains.

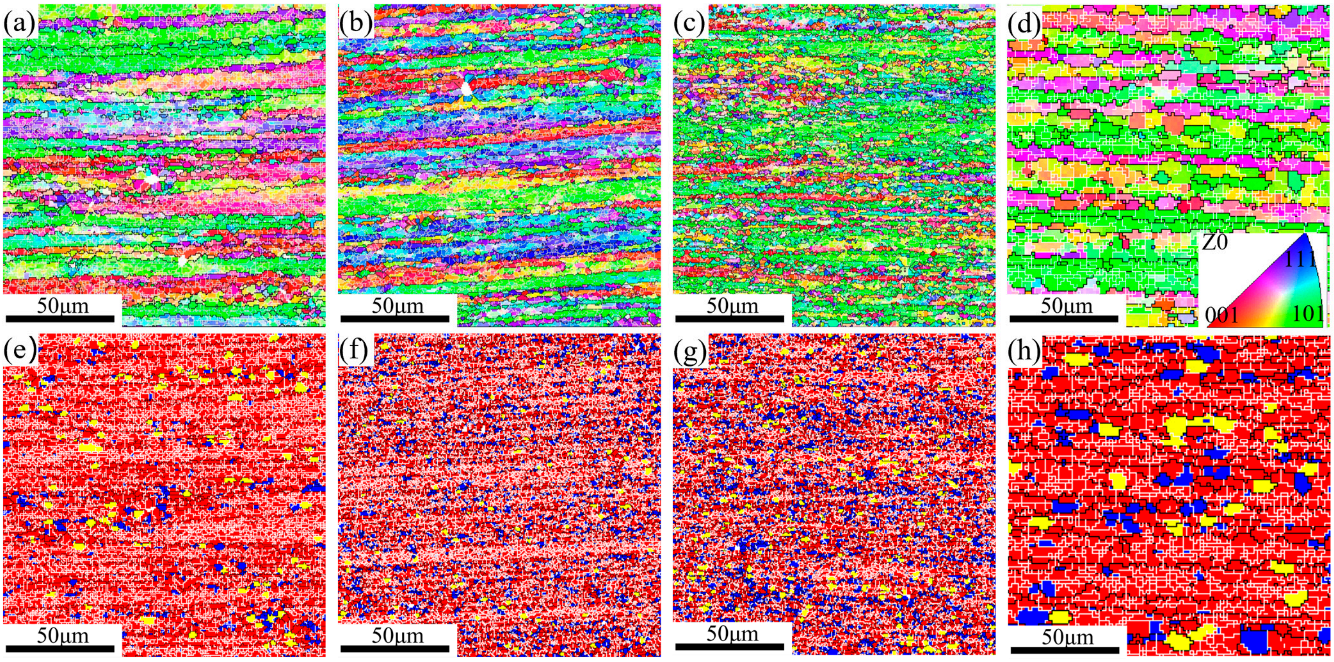

Figure 4. IPF and corresponding GOS diagram of: (**a**,**e**) as-rolled; (**b**,**f**) SEF-20; (**c**,**g**) SEF-40; (**d**,**h**) solution treated.

Figure 5 demonstrates the proportion of HAGBs (>15°), LAGBs (5–15°, including 5°), and sub-grain boundaries (SGBs, 2–5°) of the sample at different stages. Grain boundary fraction can also represent the degree of recrystallization, and the HAGB fraction corresponds to the recrystallization fraction. During the spinning extrusion process, the misorientations across the grains are increasing, and the sub-grain boundaries are constantly transformed into high-angle grain boundaries, which is a clear indication of dynamic recrystallization. However, after solution treatment, the proportion of SGBs is much higher than that of HAGBs, which suggests that the substructure is mostly maintained, and the recrystallization barely occurs during solution treatment.

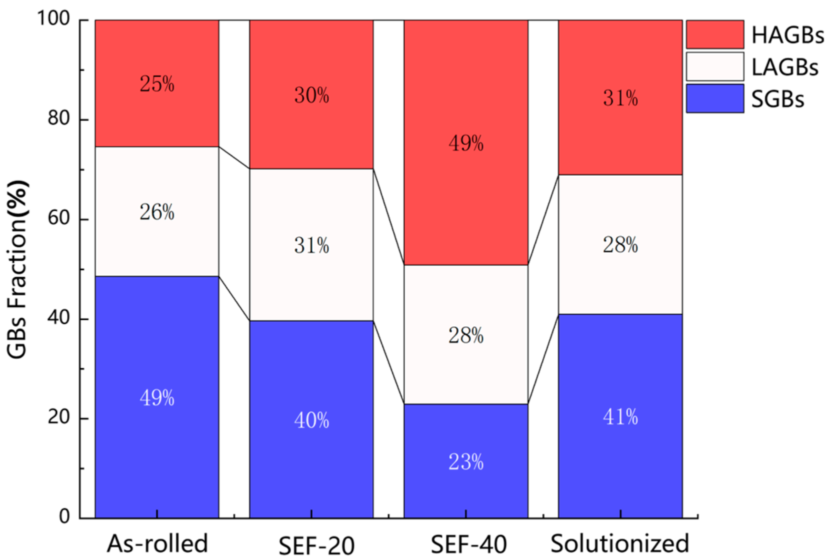

Figure 5. Grain boundary proportion in different stages of deformation.

3.2. Texture Evolution in Different Forming Stages

Figure 6 shows the orientation distribution function (ODF) diagram in different forming stages. The original rolling texture consists of brass texture, S texture, and a small amount of copper texture and cube texture. The original rolling texture type is basically unchanged during SEF, suggesting that the three-dimensional stress distribution during the SEF process is similar to that of rolling process [31,32]. This is because during the SEF process, the upper surface of the sheet is in contact with the rollers and the lower surface touches the die; thus, the material of upper and lower surfaces of the sheet experience different flow rates. This deformation process resembles that of asynchronous rolling, which is characterized by upper and lower rolls with different diameters or speeds during rolling. In the previous research on asynchronous rolling, materials will undergo shear deformation, which leads to the transformation of texture into shear texture. In this case, there is no obvious shear texture in the central part of the sheet during SEF, which indicated that the shear did not reach the center. As SEF proceeds, the brass texture {110} <112> remains as the strongest component but showed a decreasing trend during SEF. The evolution of different texture components in each forming stage is shown in Figure 7. After SEF-40, the cube texture {001} <100> is reduced by 65%, while the copper texture {112} <111> decreases by 82%, and the S texture {123} <634> decreases by 60%. Among them, the brass texture shows a slower decreasing rate compared with the other textures, and it increases sharply in the subsequent solution treatment.

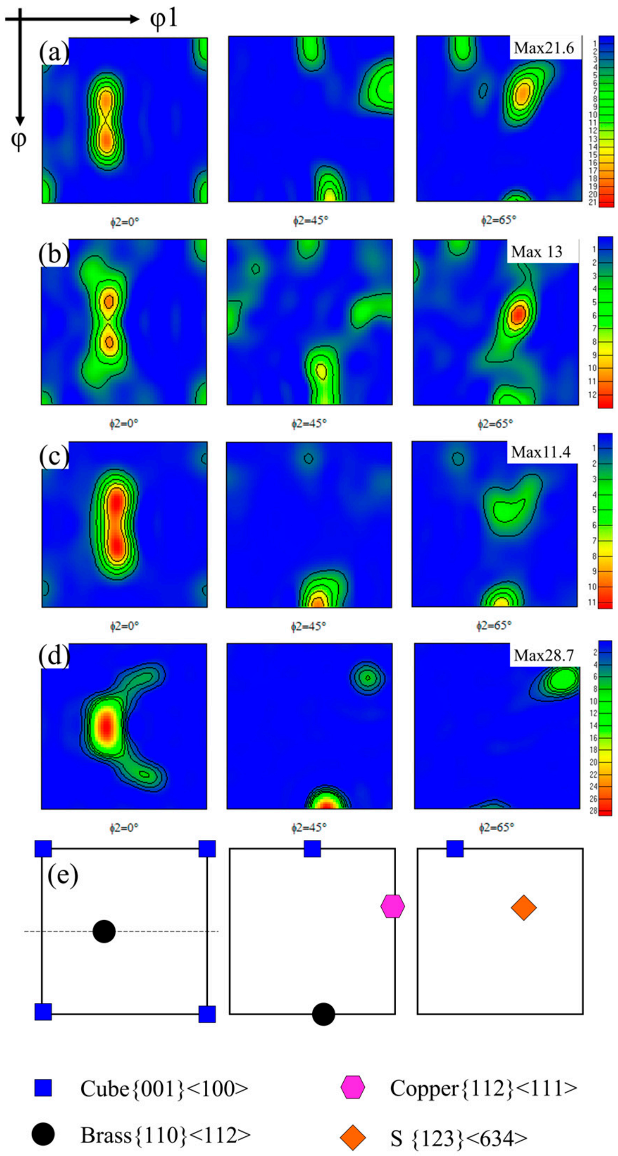

Figure 6. ODF diagram of: (**a**) as-rolled; (**b**) SEF-20; (**c**) SEF-40; (**d**) solution-treated; (**e**) distribution corresponding to ideal texture.

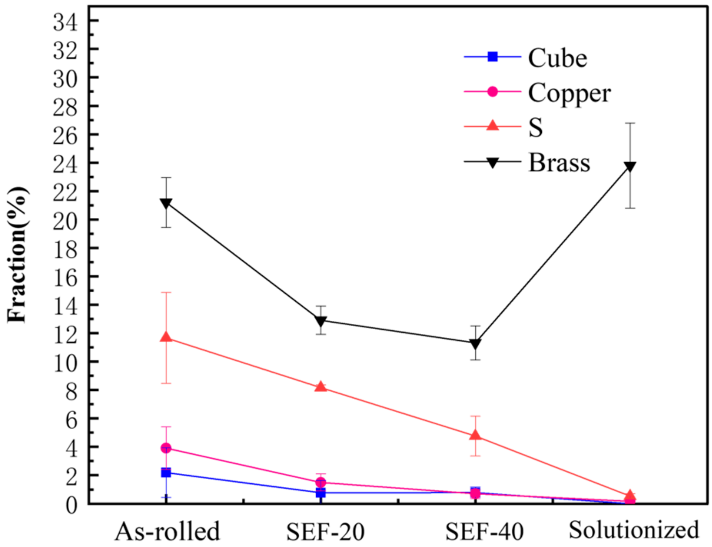

Figure 7. The statistics of texture components in each forming stage.

4. Discussion

4.1. Particle-Stimulated Nucleation (PSN)

To understand the grain configuration and texture evolution behavior of 2195 Al–Li alloy during the SEF and solution treatment, we took a closer look at its secondary phases at different stages, which play important roles in the texture evolution of the material. Figure 8 shows the SEM images of the sample in as-rolled, SEFed, and solution treatment stages, and Table 1 lists the EDS scanning results of several secondary phases. The secondary phases range from several hundreds of nanometers to 10 μm and are finely distributed in the as-rolled sample (Figure 8a). EDS suggests that these secondary phases mainly consist of θ′ phase (Al_2Cu), T2 phase (Al_6CuLi_3), and some nano-sized secondary phases. The average area fraction of the secondary phases after the SEF process remained high (5.42 ± 0.9%), which is due to the large amount of non-sharable θ′ phase.

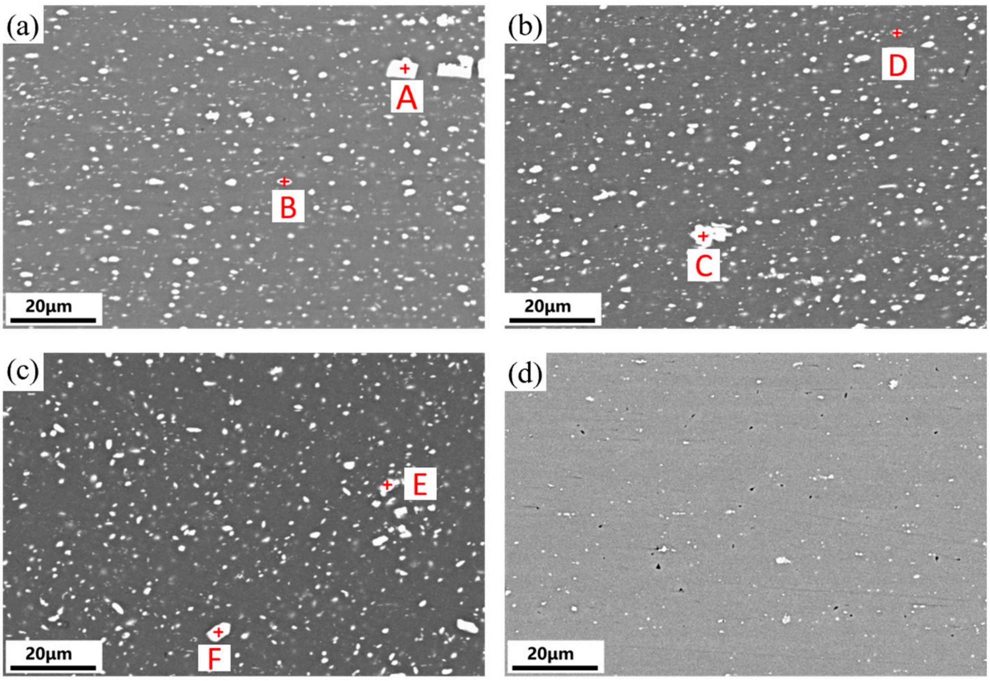

Figure 8. SEM diagram of microstructure in stage of: (**a**) as-rolled; (**b**) SEF-20; (**c**) SEF-40; (**d**) solution treated.

Table 1. EDS analysis results for the atomic ratio of elements and the corresponding close secondary phase.

Point	Al (%)	Cu (%)	Mg (%)	Ag (%)	Close Phase
A	67.3	32.1			Al_2Cu
B	86.3	13.7			Al_6CuLi_3
C	70.3	29.6			Al_2Cu
D	67.3	32.1			Al_2Cu
E	69.1	29.7	0.5	0.1	Al_2Cu
F	75.4	24.4	0.1	0.1	Al_2Cu

Figure 9a is a zoom-in EBSD micrograph near a large secondary phase in the SEF-40 sample, together with SEM and EDS elemental mapping of this region (Figure 9c). Figure 9b shows the misorientation distribution along the white arrow as marked in Figure 9a. It can be seen that the orientational difference of surrounding grains of the secondary phase is much larger than that of the matrix, and their orientations are randomized compared to the original grain structures, which is a clear indication that these large secondary phases are nucleation sites for recrystallized grains, known as particle-stimulated nucleation (PSN). This is consistent with previous studies [20,33], where large-sized secondary-phase particles facilitate the randomly oriented recrystallized grains and weaken the texture components of rolled Al alloy. It is well known that the recrystallization nucleus of PSN originates from the particle deformation zone in the vicinity of non-deforming particles. The particle deformation zone with a high dislocation density and a large orientation gradient is created during deformation due to the incompatible deformation between the non-deforming particles and the surrounding matrix. The high dislocation density and large orientation gradient in the particle deformation zone provide the force for recrystallization nucleation and growth [34]. PSN is very sensitive to particle size and spacing, and it may occur when the particle size is greater than 1 μm [35].

Moreover, we carried out STEM-EDS and TEM experiments on the nano-sized particles. Figure 9d shows the STEM image of SEF-40 sample; multiple secondary-phase particles surrounding the grains can be identified. EDS results show that these secondary-phase particles are some Ag and Mg particles that seemingly aggregate to secondary phases. It has been reported that when particles of different sizes appear in groups, dynamic recrystallization could take place even if the dimension of a single particle is smaller than the critical size for grain nucleation [35]. Therefore, secondary particles and the segregation of Mg and Ag particles in Al–Li alloy would facilitate the PSN mechanism during SEF forming, which produces a large amount of randomly oriented particles and thus weakens the texture of the material during SEF process.

4.2. Continuous Dynamic Recrystallization (CDRX)

To investigate the type of dynamic recrystallization process in SEF process. Figure 10 are TEM bright-field images and STEM of samples at different stages. It is found that with increasing deformation, massive dislocation entanglement in the as-rolled sample (Figure 10a) is rearranged and gradually transformed into dislocation walls, thus forming subgrains (Figure 10b). Upon further SEF, the sub-grain boundaries continuously absorb dislocations and the orientational difference accumulates above 15°, which consumes subgrains and finally leaves mostly high-angle recrystallized grains (Figure 10c). The aforementioned process can be categorized into classical continuous dynamic recrystallization behavior, which is an important way to coordinate deformation in alloys with dispersed particles. This is evidenced by the finely dispersed Al3Zr particles in the grains during the whole SEF process (see Figure 10c,e). These fine particles would hinder the dislocation movement during deformation process [36]. Similar microstructural evolution behavior has also been found in other Zr-containing Al–Li alloy rolled sheets [37,38]. In the study of Liu, more extensive and even CDRX was found, while in the study of Tong, similar to this paper, the continuous dynamic recrystallization was uneven and insufficient, which is obviously related to the degree of strain. Therefore, both PSN and CDRX occurs during the SEF of 2195 Al–Li alloy.

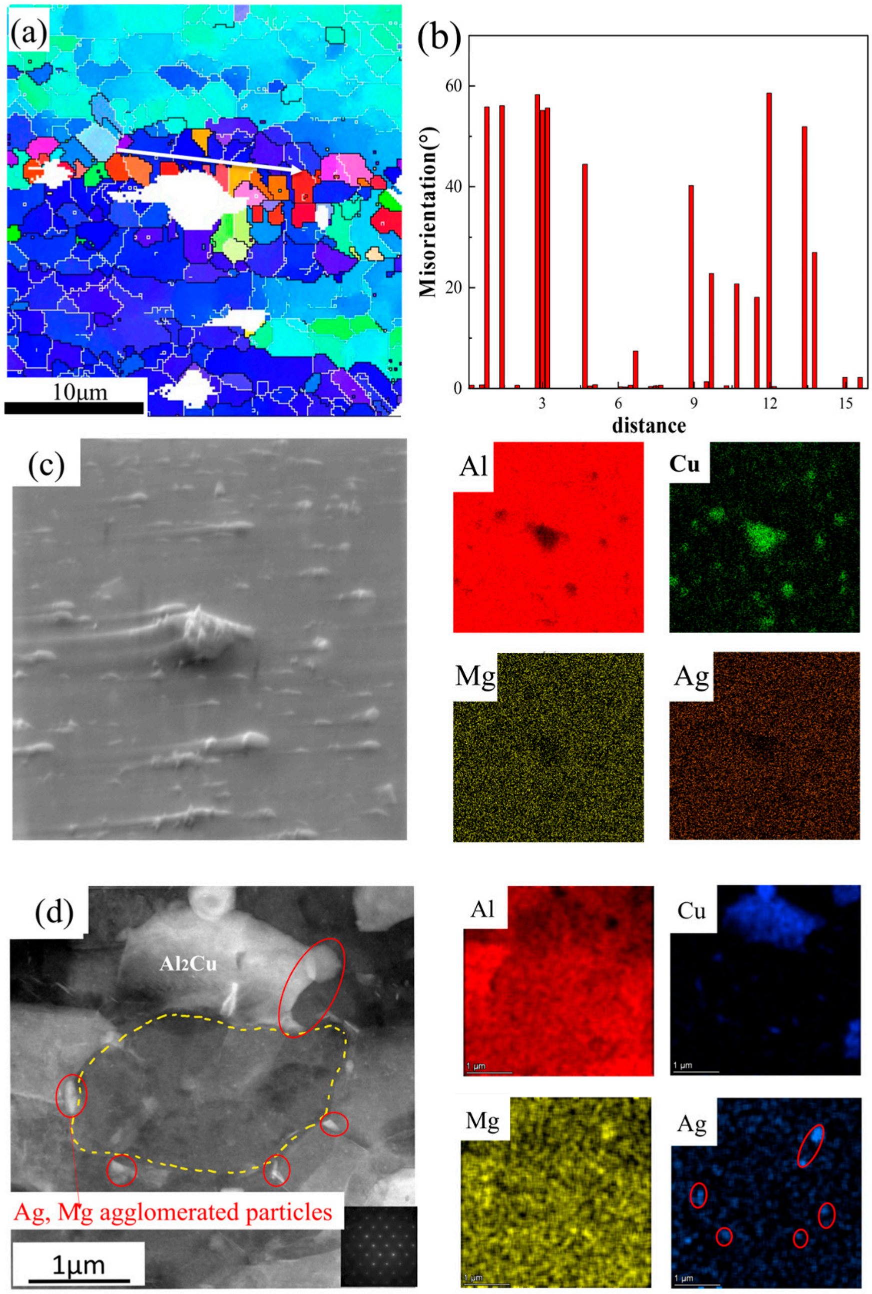

Figure 9. (**a**) EBSD and EDS near the secondary phase after SEF-40; (**b**) misorientation distribution data corresponding to the white arrow in Figure 8a; (**c**) SEM and EDS corresponding (**a**) near the secondary phase after SEF-40; (**d**) STEM-EDS near the recrystallized grains (yellow circled) after SEF-40.

4.3. Textures Evolution during SEF Process

In Section 3.2, we demonstrated that the cube texture and deformation texture (copper, Brass and S) gradually decreases during the SEF process. As shown in previous discussions, the observed reduction of the cube texture is caused by the finely dispersed Al3Zr during the SEF process (Figure 10c,d), which suppresses the recrystallization process.

PSN produces many recrystallized grains, which weakens the deformation texture [16]. However, it is interesting to note that the brass component, while showing the same decreasing trend as other texture components, was reduced to a lesser extent as the SEF proceeds (7% reduction in the second pass). This indicates that there might exist another competing effect to the PSN-induced texture weakening, which would enhance the brass component.

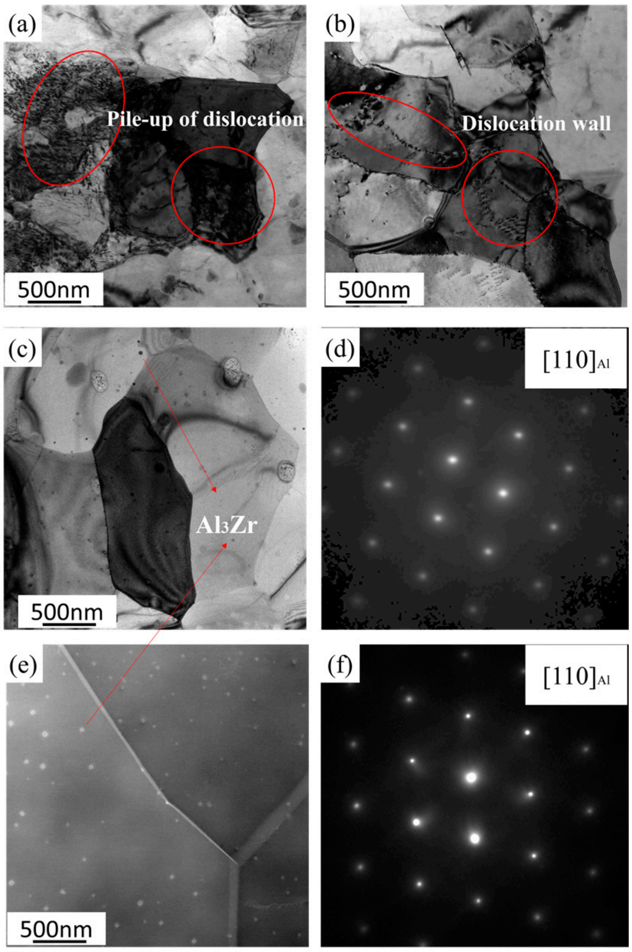

Figure 10. TEM bright-field images of: (**a**) as-rolled; (**b**) SEF-20; (**c**) SEF-40; (**d**) diffraction pattern corresponding to (**c**); (**e**) STEM of solution treated; (**f**) diffraction pattern corresponding to (**e**).

As previously demonstrated, a large amount of Al3Zr has been identified during the whole SEF process; several studies reported that Al–Li alloys with high amounts of Al3Zr all showed predominantly brass textures after rolling at different temperatures [39]; the cause of the lesser reduction of brass component could be related to the Al3Zr particles, which enhances the brass component. Liu [40] found that most recrystallized grains have {110}-orientation at the central layer of hot-rolled Al–Cu–Mg–Ag alloy sheet, which has also been observed in this work (as shown by the diffraction pattern in the Figure 10d), so the Al3Zr-facilitated continuous dynamic recrystallization explains why the brass component decreases at a lower rate than other components. Moreover, the above mechanism is also responsible for the increase of the brass component in the solution treatment, which will be discussed in the next section.

4.4. Textures Evolution during Solution Treatment

After the solution treatment, the brass texture sharply increases to about 23%, while other texture components are mostly removed. During the solution treatment, recrystallization barely occurs; this is evidenced by the similar Kernel Average Misorientation (KAM) values between the SEF-40 (KAM = 12.17) and S (KAM = 12.14) samples (Figure 11) and is consistent with the GOS data (Figure 4). In the previous discussion of the recrystallization mechanism, we found that PSN and CDRX mechanisms are competitive mechanisms in terms of their effects on texture evolution during the SEF process. The stored deformation energy is basically consumed by continuous dynamic recrystallization, which suppresses the driving force for PSN-led nucleation during solution treatment. As a result, the cube texture which is related to the recrystallization does not increase during the solution treatment [41]. In such a matrix, recrystallization is difficult to occur; the preferential growth of orientation determines the texture during solution treatment. As demonstrated before, while the grains apparently grow after solution treatment, the substructures within grains can still be observed, which suggests that the grain growth is governed by pre-existing high-angle grain boundaries. This is caused by strain-induced boundary migration (SIBM), where the difference of stored energy between both sides of the high-angle grain boundary drives the boundary migration. The rapid growth of the brass texture is therefore attributed to SIBM, which is reported to be facilitated by lamellar grain structure and the existence of Al3Zr [42,43].

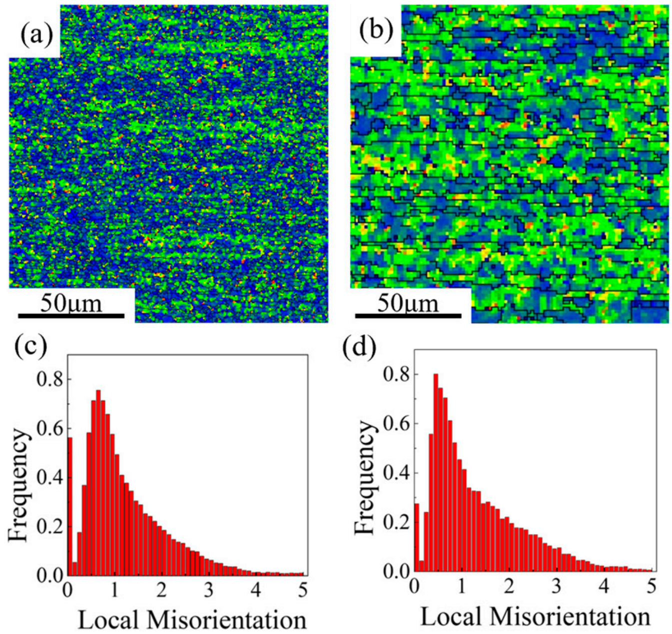

Figure 11. KAM of: (**a**,**c**) SEF-40 and (**b**,**d**) solution treated.

5. Conclusions

This work studied the microstructural and texture evolution of spinning extrusion-formed (SEFed) 2195 cylindric shell and draws the following conclusions:

1. After SEF-40, the as-rolled lamellar grains were broken up, and the fraction of recrystallized grains reached 20%. The material contains a combination of micron- and nano-sized secondary-phase particles, the former (Al_2Cu and T2 phase with aggregated Mg and Ag particles) leads to PSN, and the latter (Al3Zr particles) caused pinning of the grain boundary, which results in continuous dynamic recrystallization;
2. The deformation texture is gradually weakened by randomly oriented grains produced by PSN during SEF. The cube texture {001} <100 > decreases by 65%, the copper texture {112} < 111 > decreases by 82%, and the S texture {123} < 634 > decreases by 60%. The brass texture {110} <112 >, however, decreases slower in the second pass; this is due to the continuous dynamic recrystallization of {110}-orientation grains, which enhances the brass texture;
3. After solution treatment, basically no recrystallization occurs because of the pinning of Al3Zr. Except brass, the other deformation textures almost disappeared. The sharp increase of brass texture is caused by SIBM.

Author Contributions: X.W.: investigation, methodology, writing–original draft. W.X.: resources, conceptualization, writing—review and editing. Y.Z.: visualization, supervision, data curation. J.Z.: formal analysis, funding acquisition, data curation. All authors have read and agreed to the published version of the manuscript.

Funding: This work was supported by the National Key R&D Program of China (Grant Number 2020YFA0711104), the National Natural Science Foundation of China (Grant No. U21B6004), and the Major Project of Scientific Innovation of Hunan Province (Grant No. 2021GK1040).

Data Availability Statement: The data presented in this study are available on request from the corresponding author.

Acknowledgments: The authors would like to take this opportunity to express their appreciation to the National Key R&D Program of China (No. 2020YFA0711104), the National Natural Science Foundation of China (Grant No. U21B6004), and the Major Project of Scientific Innovation of Hunan Province (Grant No. 2021GK1040).

Conflicts of Interest: The authors declare no conflict of interest.

References

1. El-Aty, A.A.; Xu, Y.; Zhang, S.; Ma, Y.; Chen, D. Experimental investigation of tensile properties and anisotropy of 1420, 8090 and 2060 Al-Li alloys sheet undergoing different strain rates and fibre orientation: A comparative study. *Procedia Eng.* **2017**, *2017*, 13–18. [CrossRef]
2. Ahmed, B.; Wu, S.J. Aluminum Lithium Alloys (Al-Li-Cu-X)-New Generation Material for Aerospace Applications. *Appl. Mech. Mater.* **2013**, *440*, 104–111. [CrossRef]
3. Betsofen, S.Y.; Antipov, V.V.; Knyazev, M.I. Al–Cu–Li and Al–Mg–Li alloys: Phase composition, texture, and anisotropy of mechanical properties (Review). *Russ. Metall.* **2016**, *2016*, 326–341. [CrossRef]
4. Xia, Q.; Long, J.; Xiao, G.; Yuan, S.; Qin, Y. Deformation mechanism of ZK61 magnesium alloy cylindrical parts with longitudinal inner ribs during hot backward flow forming. *J. Mater. Process. Technol.* **2021**, *296*, 117197. [CrossRef]
5. Xu, H.Q.; Li, M.Z.; Li, L.L.; Zhang, R.; Wang, D.L.; Liang, W.; Shen, Y.J. Power Spinning Study of Thin-Walled 5A06 Aluminum Alloy Cylinder with Longitudinal and Hoop Inner Ribs for Manufacturing Engineering. *Adv. Mater. Res.* **2012**, *583*, 301–305. [CrossRef]
6. Garmestania, H.; Kalidindib, S.R.; Williamsa, L.; Bacaltchuk, C.M.; Fountain, C.; Lee, E.W.; Es-Said, O.S. Modeling the evolution of anisotropy in Al–Li alloys: Application to Al–Li 2090-T8E41. *Int. J. Plast.* **2002**, *18*, 1373–1393. [CrossRef]
7. Gondo, S.; Arai, H.; Kajino, S.; Hanada, K. Evolution of texture distribution in thickness direction of aluminum sheet in metal spinning. *Mater. Charact.* **2022**, *188*, 111877. [CrossRef]
8. Rakshit, R.; Sarkar, A.; Panda, S.K.; Mandal, S. Influence of out-of-plane stretch forming induced different strain paths on micro-texture evolution, slip system activity and Taylor factor distribution in Al–Li alloy. *Mater. Sci. Eng. A* **2022**, *830*, 142267. [CrossRef]
9. Li, S.; Zhao, Q.; Liu, Z.; Li, F. A Review of Texture Evolution Mechanisms During Deformation by Rolling in Aluminum Alloys. *J. Mater. Eng. Perform.* **2018**, *27*, 3350–3373. [CrossRef]
10. Wang, X.; Liu, H.; Tang, X.; Wang, Y.; Guo, M.; Zhuang, L. Influence of asymmetric rolling on the microstructure, texture evolution and mechanical properties of Al–Mg–Si alloy. *Mater. Sci. Eng. A* **2022**, *844*, 143154. [CrossRef]
11. Ma, Y.-l.; Li, J.-f.; Zhang, R.-z.; Tang, J.-g.; Huang, C.; Li, H.-y.; Zheng, Z.-q. Strength and structure variation of 2195 Al-Li alloy caused by different deformation processes of hot extrusion and cold-rolling. *Trans. Nonferrous Met. Soc. China* **2020**, *30*, 835–849. [CrossRef]
12. Jata, K.V.; Singh, A.K. Texture and Its Effects on Properties in Aluminum–Lithium Alloys. In *Aluminum-Lithium Alloys*; Butterworth-Heinemann: Oxford, UK, 2014; pp. 139–163.
13. Xie, Y.; Deng, Y.; Wang, Y.; Guo, X. Effect of asymmetric rolling and subsequent ageing on the microstructure, texture and mechanical properties of the Al-Cu-Li alloy. *J. Alloys Compd.* **2020**, *836*, 155445. [CrossRef]
14. Bate, P.S.; Ridley, N.; Zhang, B. Mechanical behaviour and microstructural evolution in superplastic Al-Li-Mg-Cu-Zr AA8090. *Acta Mater.* **2007**, *55*, 4995–5006. [CrossRef]
15. Wang, Y.X.; Zhao, G.Q.; Xu, X.; Chen, X.X. Effect of extrusion parameters on microstructure, texture and mechanical property anisotropy of spray deposited 2195 Al-Li alloy profile. *Mater. Sci. Eng. A-Struct. Mater. Prop. Microstruct. Process.* **2021**, *818*, 19. [CrossRef]
16. Duan, S.; Guo, F.; Zhang, Y.; Chong, K.; Lee, S.; Matsuda, K.; Zou, Y. Effects of texture and precipitates characteristics on anisotropic hardness evolution during artificial aging for an Al–Cu–Li alloy. *Mater. Des.* **2021**, *212*, 110216. [CrossRef]
17. Wang, X.-Y.; Jiang, J.-T.; Li, G.-A.; Wang, X.-M.; Shao, W.-Z.; Zhen, L. Particle-stimulated nucleation and recrystallization texture initiated by coarsened Al_2CuLi phase in Al–Cu–Li alloy. *J. Mater. Res. Technol.* **2021**, *10*, 643–650. [CrossRef]
18. Zhao, Q.; Liu, Z.; Wahab, M.A. Enhanced Brass texture of hot-rolled Al-4Cu-1.6Mg alloy by 0.1% Zr addition. *Mater. Charact.* **2020**, *169*, 110643. [CrossRef]
19. Yang, S.; Liu, L.; Gao, F.; Xu, Z.; Song, D.; Jiang, P. Evolution of texture and precipitates in Al–Cu–Li alloy during deformation and heat treatment and its effect on anisotropy. *Mater. Res. Express* **2021**, *8*, 056509. [CrossRef]
20. Zang, Q.; Chen, H.; Lee, Y.-S.; Yu, H.; Kim, M.-S.; Kim, H.-W. Improvement of anisotropic tensile properties of Al-7.9Zn-2.7Mg-2.0Cu alloy sheets by particle stimulated nucleation. *J. Alloys Compd.* **2020**, *828*, 154330. [CrossRef]

21. She, H.; Shu, D.; Dong, A.; Wang, J.; Sun, B.; Lai, H. Relationship of particle stimulated nucleation, recrystallization and mechanical properties responding to Fe and Si contents in hot-extruded 7055 aluminum alloys. *J. Mater. Sci. Technol.* **2019**, *35*, 2570–2581. [CrossRef]
22. Wang, X.; Guo, M.; Moliar, O.; Peng, W.; Xie, C.; Chen, J.; Wang, Y. Enhanced grain refinement and texture weakening in Al–Mg–Si alloy through a novel thermomechanical processing. *J. Alloys Compd.* **2022**, *925*, 166654. [CrossRef]
23. Chen, X.; Zhao, G.; Xu, X.; Wang, Y. Effects of heat treatment on the microstructure, texture and mechanical property anisotropy of extruded 2196 Al-Cu-Li alloy. *J. Alloys Compd.* **2021**, *862*, 158102. [CrossRef]
24. Khani Moghanaki, S.; Kazeminezhad, M.; Logé, R. Effect of concurrent precipitation on the texture evolution during continuous heating of multi directionally forged solution treated Al-Cu-Mg alloy. *Mater. Charact.* **2017**, *131*, 399–405. [CrossRef]
25. Wang, X.-f.; Guo, M.-x.; Peng, W.-f.; Wang, Y.-g.; Zhuang, L.-z. Relationship among solution heating rate, mechanical properties, microstructure and texture of Al−Mg−Si−Cu alloy. *Trans. Nonferrous Met. Soc. China* **2021**, *31*, 36–52. [CrossRef]
26. Liu, T.L.; Li, H.R.; Ma, Y.L.; Li, J.F.; Liu, D.Y.; Lu, D.D.; Guo, Y.J. Investigation of anisotropy and structure variation of spray-formed 2195 Al-Li alloy via final temperature-controlled rolling and cold rolling. *J. Alloys Compd.* **2023**, *937*, 168414. [CrossRef]
27. Zhang, J.X.; Ma, M.; Liu, W.C. Effect of initial grain size on the recrystallization and recrystallization texture of cold-rolled AA 5182 aluminum alloy. *Mater. Sci. Eng. A-Struct. Mater. Prop. Microstruct. Process.* **2017**, *690*, 233–243. [CrossRef]
28. Rometsch, P.A.; Zhang, Y.; Knight, S. Heat treatment of 7xxx series aluminium alloys—Some recent developments. *Trans. Nonferrous Met. Soc. China* **2014**, *24*, 2003–2017. [CrossRef]
29. Sidor, J.J.; Decroos, K.; Petrov, R.H.; Kestens, L.A.I. Evolution of recrystallization textures in particle containing Al alloys after various rolling reductions: Experimental study and modeling. *Int. J. Plast.* **2015**, *66*, 119–137. [CrossRef]
30. Li, X.-y.; Xia, W.-j.; Chen, J.-h.; Yan, H.-g.; Li, Z.-z.; Su, B.; Song, M. Dynamic recrystallization, texture and mechanical properties of high Mg content Al–Mg alloy deformed by high strain rate rolling. *Trans. Nonferrous Met. Soc. China* **2021**, *31*, 2885–2898. [CrossRef]
31. Luo, W.; Chen, F.; Xu, B.; Yang, Z.; Guo, Y.; Lu, B.; Huang, T. Study on compound spinning technology of large thin-walled parts with ring inner ribs and curvilinear generatrix. *Int. J. Adv. Manuf. Technol.* **2018**, *98*, 1199–1216. [CrossRef]
32. Zeng, X.; Fan, X.G.; Li, H.W.; Zhan, M.; Li, S.H.; Wu, K.Q.; Ren, T.W. Heterogeneous microstructure and mechanical property of thin-walled tubular part with cross inner ribs produced by flow forming. *Mater. Sci. Eng. A* **2020**, *790*, 139702. [CrossRef]
33. Zhang, Y.; Juul Jensen, D.; Zhang, Y.; Lin, F.; Zhang, Z.; Liu, Q. Three-dimensional investigation of recrystallization nucleation in a particle-containing Al alloy. *Scr. Mater.* **2012**, *67*, 320–323. [CrossRef]
34. Schäfer, C.; Song, J.; Gottstein, G. Modeling of texture evolution in the deformation zone of second-phase particles. *Acta Mater.* **2009**, *57*, 1026–1034. [CrossRef]
35. Humphreys, J.; Rohrer, G.S.; Rollett, A. Recrystallization of Two-Phase Alloys. In *Recrystallization and Related Annealing Phenomena*; Pergamon Press: Oxford, Uk, 2017; pp. 321–359.
36. Wang, K.; Yin, D.; Zhao, Y.-C.; Atrens, A.; Zhao, M.-C. Microstructural evolution upon heat treatments and its effect on corrosion in Al-Zn-Mg alloys containing Sc and Zr. *J. Mater. Res. Technol.* **2020**, *9*, 5077–5089. [CrossRef]
37. Liu, Q.; Huang, X.; Yao, M.; Yang, J. On deformation-induced continuous recrystallization in a superplastic Al-Li-Cu-Mg-Zr alloy. *Acta Metall. Et Mater.* **1992**, *40*, 1753–1762. [CrossRef]
38. Tong, M.; Jiang, F.; Wang, H.; Jiang, J.; Wu, M.; Tang, Z. The evolutions of flow stress and microstructure of Al-Mg-Mn-Sc-Zr alloy at elevated temperatures. *Mater. Charact.* **2021**, *182*, 111560. [CrossRef]
39. Mondal, C.; Singh, A.K.; Mukhopadhyay, A.K.; Chattopadhyay, K. Formation of a single, rotated-Brass {110} <556> texture by hot cross-rolling of an Al-Zn-Mg-Cu-Zr alloy. *Scr. Mater.* **2011**, *64*, 446–449. [CrossRef]
40. Liu, F.; Liu, Z.; Jia, P.; Bai, S.; Yan, P.; Hu, Y. Dynamic dissolution and texture evolution of an Al–Cu–Mg–Ag alloy during hot rolling. *J. Alloys Compd.* **2020**, *827*, 154254. [CrossRef]
41. Doherty, R.D.; Hughes, D.A.; Humphreys, F.J.; Jonas, J.J.; Jensen, D.J.; Kassner, M.E.; King, W.E.; McNelley, T.R.; McQueen, H.J.; Rollett, A.D. Current issues in recrystallization: A review. *Mater. Sci. Eng. A* **1997**, *238*, 219–274. [CrossRef]
42. Zhao, Q.; Liu, Z.Y. Texture Evolution of Hot Rolled Al-Cu-Mg-Zr Alloy During Annealing. *Met. Mater. Int.* **2022**, *28*, 2947–2961. [CrossRef]
43. Tsivoulas, D.; Prangnell, P.B. The effect of Mn and Zr dispersoid-forming additions on recrystallization resistance in Al-Cu-Li AA2198 sheet. *Acta Mater.* **2014**, *77*, 1–16. [CrossRef]